Bull. Chem. Soc. Ethiop. **2027**, 41(1), 1-13.
DOI: https://dx.doi.org/10.4314/bcse.v41i1.1

ISSN 1011-3924
Printed in Ethiopia
Online ISSN 1726-801X
© 2027 Chemical Society of Ethiopia and The Authors

CORE-SHELL In@In_2O_3 NPs FROM ROSEMARY EXTRACT AND BIOACTIVITY STUDY

Ali Mohammed Al-Tamimi[1] and Waleed Khalid Mahdi[*2]

[1,2*]Department of Chemistry, College of Education for Pure Science, Ibn -Al-Haitham, University of Baghdad, Baghdad, Iraq

(Received March 4, 2026; Revised July 27, 2026; Accepted September 30, 2026)

ABSTRACT. In this study, a phytochemical-mediated synthesis approach was used to prepare indium oxide-coated indium nanoparticles (In@In_2O_3NPs). This environmentally friendly method employed aqueous rosemary extract rich in bioactive phytochemicals that act as reducing, capping, and stabilizing agents during NPs synthesis. The NPs were characterized using FTIR, XRD, EDX, FESEM, TEM, BET, and zeta potential. The particle size was 10-60 nm, and they were irregularly spherical. The specific surface area determined by BET analysis was 128.53 m^2/g. The zeta potential was -39.9 mV, indicating strong electrostatic repulsion between the particles, thereby ensuring their stability and preventing agglomeration. Bioactivity was measured against *Staphylococcus aureus*, *Enterococcus faecalis*, *Streptococcus mutans*, and *Escherichia coli*. The minimum inhibitory concentrations (MICs) and sub-MICs of In@In_2O_3 NPs were found to be 234.38, 234.38, 117.19, and 234.38 µg/mL, and 117.19, 117.19, 58.60, and 117.19 µg/mL, respectively. At a concentration of 234.38 µg/mL, the In@In_2O_3 NPs exhibited low toxicity (5.6%). The tested bacterial isolates exhibited weak to moderate biofilm-forming ability, and In@In_2O_3 NPs effectively inhibited biofilm formation. The antioxidant activity of the resulting NPs was examined using the DPPH assay. A relationship was found between the concentration of the In@In_2O_3 NPs solution and the inhibition rate, with inhibition increasing as the concentration increased.

KEY WORDS: Phytochemical-mediated synthesis, In@In_2O_3 nanoparticle, Rosemary, Bioactivity

INTRODUCTION

In recent years, scientific interest has grown in the environmentally friendly fabrication of nanoparticles (NPs) using plant extracts that act as reducing, stabilizing, and coating agents. One such extract is rosemary, which has garnered significant attention in numerous studies due to its medicinal properties, including its antioxidant, antimicrobial, and anti-inflammatory effects. Rosemary is an aromatic, evergreen shrub belonging to the mint family (Lamiaceae), and it is rich in bioactive compounds, including rosmarinic acid, carnosol, and carnosic acid [1-3]. The NPs possess unique chemical and physical properties dependent on their size and surface area, including catalytic activity, electrical conductivity, and other essential characteristics for diverse and important applications, particularly in the medical field, where they are used in cancer treatment and drug delivery systems [4, 5]. In the environmental field, NPs have been widely applied in water treatment, including pollutant removal and the restoration of aquatic ecosystems [6, 7]. Among the various nanomaterials, core -shell NPs have garnered increasing attention from researchers due to their unique properties and wide-ranging applications in the medical, optical, and environmental fields. These properties can be modified by altering the composition of the core and shell materials or by adjusting the coating thickness [8, 9]. Furthermore, indium NPs have attracted considerable attention because of their unique optical and electronic properties, good chemical stability, and relatively low toxicity, which make them promising materials for various technological applications. Different synthesis strategies have been reported for producing indium NPs, including liquid-phase dispersion [10] and pulsed laser ablation [11]. Moreover, controlled oxidation of metallic indium has been successfully used to prepare

*Corresponding author. E-mail: waleed.k.m@ihcoedu.uobaghdad.edu.iq
This work is licensed under the Creative Commons Attribution 4.0 International License

$In@In_2O_3$ core–shell nanostructures with enhanced photocatalytic activity [12]. Meanwhile, bacterial resistance to many antibiotics has recently increased. Previous studies have confirmed that antibiotic-resistant bacteria are responsible for a substantial proportion of hospital-acquired infections [13,14]. Bacteria regulate and coordinate biofilm formation, protecting themselves from harsh environmental conditions and antibiotics [15]. Several researchers have confirmed the ability of NPs to inhibit quorum-sensing molecules (the mechanisms that enable bacteria to form biofilms), thus preventing their formation [16-18]. In this study, $In@In_2O_3$ core–shell NPs were synthesized using rosemary extract, whose bioactive polyphenols served as reducing and stabilizing agents during the phytochemical-mediated synthesis process. The antibacterial and biofilm-forming activity of the synthesized NPs was investigated as a potential strategy for inhibiting biofilm formation and helping to overcome bacterial resistance to antibiotics.

EXPERMENTAL

Materials

Rosemary was obtained from a local nursery. The following chemicals were used: hydrated indium sulphate (CDH, India), sodium hydroxide (Loba Chemie, India), sodium borohydride (Sigma-Aldrich, St. Louis, MO, USA), deionized water (Rafidain Environment Office, Iraq), absolute ethanol (Riedel-de Haën, Germany), absolute methanol (SRL, Maharashtra, India), nutrient broth (HiMedia Laboratories, India), Mueller–Hinton broth (Accumix, Spain), sodium resazurin salt (Sigma-Aldrich, USA), 0.9% isotonic saline (Sigma-Aldrich, USA), Triton X-100 (Sigma-Aldrich, USA), crystal violet (HiMedia Laboratories, India), and 1,1-diphenyl-2-picrylhydrazyl (DPPH) (Sigma-Aldrich, USA).

Instrumentation

The following instruments were used in this study. Fourier-transform infrared (FTIR) spectroscopy (Shimadzu, Japan) was used to identify the functional groups present in the rosemary extract and on the surface of the synthesized NPs. Ultraviolet–visible (UV–Vis) spectroscopy (Shimadzu, Japan) was used to monitor NPs formation. X-ray diffraction (XRD, Shimadzu, Japan) was employed to determine the crystalline phases and crystal structure of the synthesized NPs. Field emission scanning electron microscopy (FESEM, Carl Zeiss, Germany) and transmission electron microscopy (TEM, Carl Zeiss, Germany) were used to examine the morphology and particle size of the NPs, while energy-dispersive X-ray spectroscopy (EDX, Carl Zeiss, Germany) was used to determine their elemental composition. Atomic force microscopy (AFM, SPM AA3000, USA) was used to investigate the surface topography of the NPs. The specific surface area was measured using a Brunauer–Emmett–Teller (BET) surface area analyzer (Micromeritics, USA). Surface charge and colloidal stability were evaluated using a zeta potential analyzer (Brookhaven Instruments Corporation, USA). Bacterial identification was performed using the VITEK® 2 system (bioMérieux, France). An autoclave (Hirayama, Japan), incubator (Fisher Scientific, USA), centrifuge (Daihan Labtech, South Korea), hotplate stirrer (Daihan Labtech, South Korea), oven (Daihan Labtech, South Korea), and ultrasonic bath (Germany) were used during nanoparticle synthesis and microbiological experiments. An ELISA microplate reader (BioTek, USA) was used to measure absorbance during the broth microdilution antibacterial assay and the biofilm inhibition assay. A UV–Vis spectrophotometer (Shimadzu, Japan) was used to measure absorbance during the DPPH antioxidant and hemolysis assays.

Preparation of plant extract

Fresh rosemary was obtained from local nurseries in Iraq. The leaves were washed and rinsed with deionized water, dried, and ground into a fine powder. About 500 mL of deionized water was mixed with 50 g of powdered rosemary leaves and stirred constantly for 30 min at 50 °C. The mixture was filtered, and the filtrate was centrifuged at 4000 rpm for 15 min, yielding a yellow aqueous extract with a pH of 6.

Phytochemical-mediated synthesis of core- shell In@In_2O_3 nanoparticles

First, 1 g (1.47 mmol) of hydrated indium sulfate, $In_2(SO_4)_3 \cdot 9H_2O$, was dissolved in 100 mL of deionized water by heating and stirring at 70 °C for 30 min. Subsequently, 100 mL of the previously prepared aqueous rosemary extract was added to the indium sulfate solution, and the resulting mixture was maintained at 70 °C under continuous stirring for an additional 30 min. Then, a 0.1 M NaOH solution was added dropwise to the mixture until the pH reached 12, causing the solution to turn yellow. Subsequently, 15 mmol (0.57 g) of sodium borohydride ($NaBH_4$) was added as an excess reducing agent. Upon continuous stirring, the color of the reaction mixture changed from yellow to gray, indicating the formation of In@In_2O_3 NPs. The reaction mixture was allowed to stand for 24 h, after which the NPs were collected by filtration. The precipitate was washed several times with deionized water, followed by absolute ethanol, and then dried in a vacuum oven at 250 °C for 3 h. After drying, approximately 0.30 g of gray In@In_2O_3 NPs was obtained, corresponding to an approximate yield of 89%, calculated with respect to the initial indium content in the precursor salt.

Studies of bioactivity

Microtiter plate method for minimum inhibitory concentration (MIC) with Resazurin

The minimum inhibitory concentration (MIC) was determined using the broth microdilution method in a 96-well microtiter plate (CLSI, 2020; document M07). This was done in compliance with the requirements established by the Clinical and Laboratory Standards Institute (CLSI). The bacterial suspensions were adjusted to approximately 5×10^5 CFU/mL after repeated twofold dilutions of each chemical (7500, 3750, 1875, 937.5, 468.75, 234.38, 117.19, 58.60, 29.30, and 14.65 µg/mL) were prepared in Mueller-Hinton broth. Each well received 20 µL of 0.01% resazurin solution after the plate was incubated for 24 hr. at 37 °C. This dye allows for a noticeable colour change. A colour change from blue to pink signified bacterial growth, and wells that did not experience this change were considered growth-inhibited. Because of this, the minimum inhibitory concentration, also known as the MIC, is the lowest concentration at which there is no colour change [19].

Toxicity

A hemolysis experiment assessed the toxicity of the In@In_2O_3 NPs produced. Plasma was separated by centrifugation at 3000 rpm for 5 min, yielding fresh red blood cells (RBCs). The RBCs were washed multiple times with normal saline and resuspended to a 2% hematocrit. In equal amounts, NPs and a red blood cell suspension (at the minimal inhibitory concentration) were incubated at 37 °C for 1 hr. The centrifuge was run for 10 min at 1500 rpm. To measure hemoglobin release, the absorbance of the supernatant was measured at 540 nm. The positive control was 0.1% Triton X-100 with RBCs, while the negative control was saline containing RBCs [20, 21].

Formation of biofilms and anti-biofilm actions

Biofilm formation was done using a 96-well microtiter plate [22]. Three wells were cultured for 24 hr. at 37 °C after receiving 200 µL of nutrient broth and 5-10 µL of bacteria. After the incubation, the wells were thoroughly rinsed with deionized water several times and allowed to dry. A thin biofilm layer developed. After 200 µL of absolute methanol was added for a few minutes, the wells were removed and left to air-dry completely for 15 min. 200 µL of 0.5% crystal violet was then added to each well. The wells were thoroughly cleaned and dried again. Lastly, the optical density (OD) was measured at 630 nm after 10-15 minutes, using 200 µL of absolute ethanol. Three wells containing only nutrient broth were used to measure the negative control. According to Table 1 [23], all treated isolates were categorized as weak or moderate biofilm producers based on optical density (OD) and optical density control (ODC) values. The experiment was repeated using identical procedures to determine whether the NPs produced could prevent biofilm formation. However, before incubation, 100 µL of nutrient broth and the MIC concentration of the produced NPs were introduced in place of 200 µL of nutrient broth. Equation (1) below was used to determine the inhibition percentage after the optical density was measured and compared to the negative and positive control groups:

$$\text{Inhibition}\% = \frac{\text{OD}_{\text{control}-}\ \text{OD}_{\text{treated}}}{\text{OD}_{\text{control}-}\ \text{OD}_{\text{blank}}} \times 100\% \quad (1)$$

Table 1. Biofilm intensity based on the OD and ODc values.

OD value	Biofilm intensity
OD ≤ ODc	Non-producer
ODc < OD ≤ 2X ODc	Weak
2ODC < OD < 4ODC	Moderate
OD > 4X ODc	Strong

Properties of antioxidants

A standard antioxidant test uses the 1,1-diphenyl-2-picrylhydrazyl (DPPH) free radical. A DPPH solution was prepared at 1 mmol in methanol. Various concentrations of nanoparticle solution (25, 50, 75, and 100 µg/mL) were combined with equal amounts of DPPH solution. After 30 min of dark swirling, the solution was measured for absorbance at 517 nm. DPPH and ascorbic acid were positive controls, while only DPPH was the negative control. The free radical scavenging activity was determined using the following Equation (2) [24].

$$\text{DPPH radical scavenging activity}\ (\%) = \frac{A0-As}{A0} \times\ 100\% \quad (2)$$

Where A0 and As represent the absorbance values for the corresponding blank and sample.

RESULTS AND DISCUSSION

FTIR spectroscopy

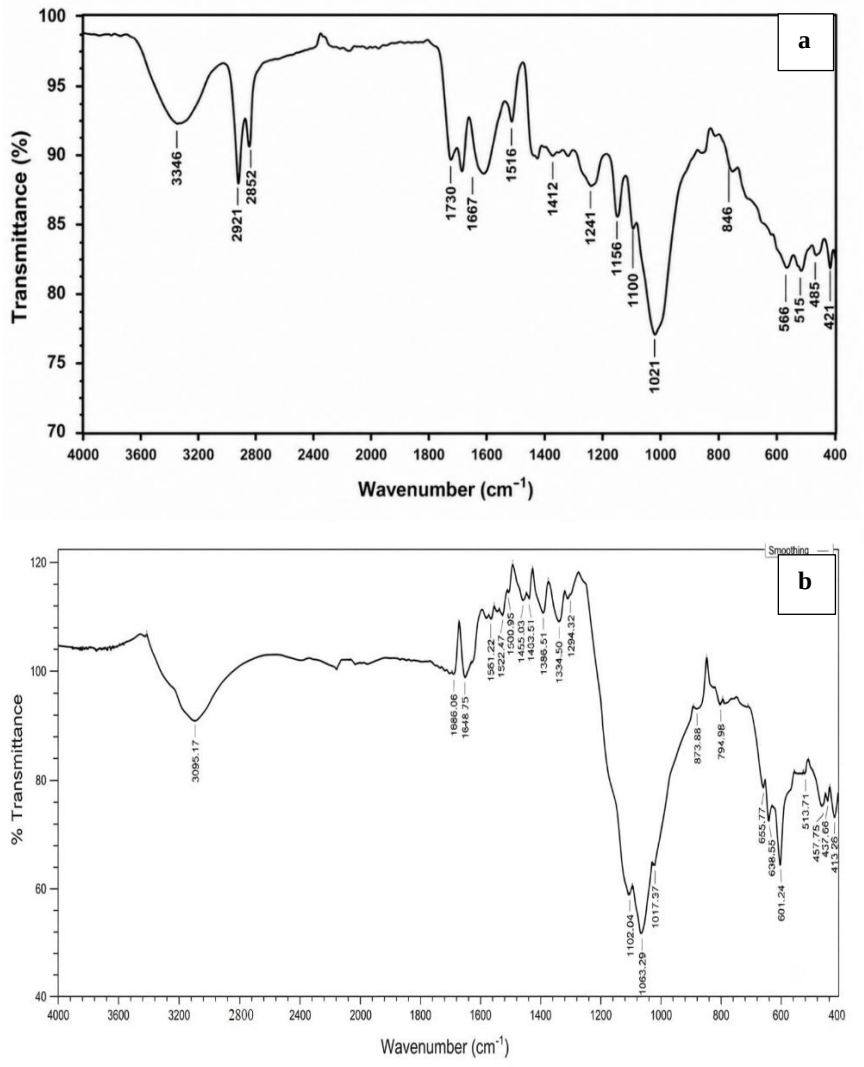
This approach was used to identify functional groups. Both rosemary extract (Figure 1(a)) and indium sulfate salt hydrate (Figure 1(b)) exhibit the loss of significant functional groups in the salt and the plant as a result of the production of In@In_2O_3 NPs (Figure 1(c)).

Figure 1(a). The broad absorption band at 3346 cm^{-1} is attributed to the stretching vibration of hydroxyl (O–H) groups, while the bands at 2921 and 2852 cm^{-1} correspond to the asymmetric and symmetric stretching vibrations of aliphatic C–H (CH_2 and CH_3) groups, respectively. The absorption bands at 1156, 1100, and 1021 cm^{-1} are assigned to C–O stretching vibrations, whereas

the bands at 1730 and 1667 cm^{-1} are attributed to the stretching vibrations of carbonyl (C=O) groups [25].

Figure 1(b). The broad band observed at 3286 cm^{-1} is assigned to the stretching vibration of hydroxyl (O–H) groups from adsorbed water molecules. The characteristic absorption bands in the regions of 1100-1200 cm^{-1} and 960-1190 cm^{-1} are attributed to the asymmetric and symmetric stretching vibrations of sulfate (SO_4^{2-}) groups, respectively [26].

Figure 1(c) presents the FT-IR spectrum of the synthesized In@In_2O_3 NPs. The disappearance of the characteristic sulfate bands, together with the reduction in the intensity of the bands associated with the rosemary extract, indicates the successful formation of the NPs. In addition, the absorption bands observed in the 400-600 cm^{-1} region are assigned to In–O stretching vibrations, confirming the presence of indium oxide in the synthesized core–shell NPs [27].



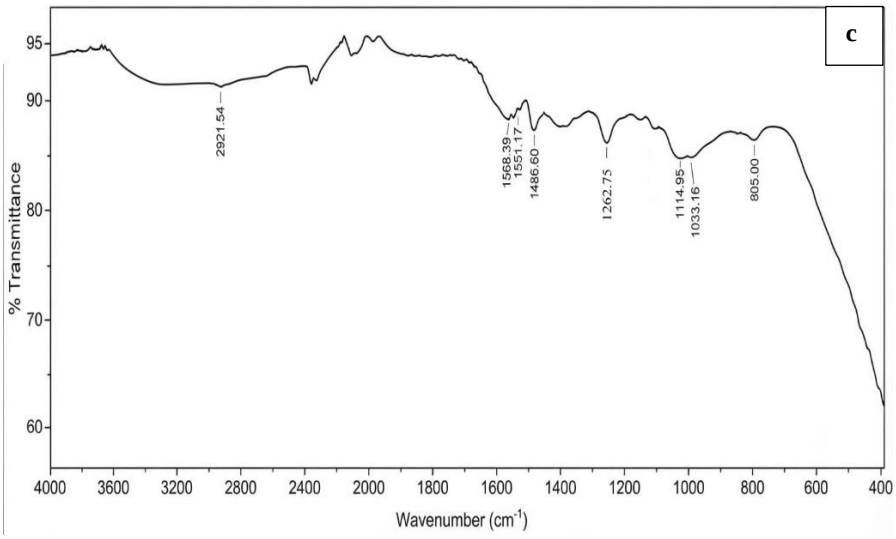


Figure. 1 FTIR spectrum of (a) rosemary extract. (b) $In_2(SO_4)_3.9H_2O$. (c) $In@In_2O_3$ NPs.

UV-Vis spectroscopy

The UV–Vis spectroscopy measurement was performed using an aqueous suspension of the synthesized $In@In_2O_3$ NPs. As shown in Figure 2, a characteristic absorption band at 268 nm is attributed to the surface plasmon resonance (SPR) of indium NPs [28]. In addition, a broad absorption band in the range of 300-350 nm is assigned to the In_2O_3 shell [29]. These spectral features support the formation of core–shell $In@In_2O_3$ NPs.

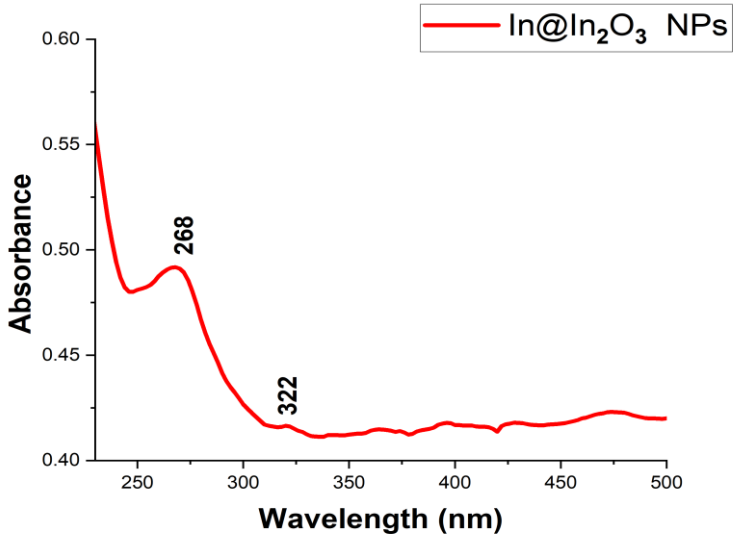
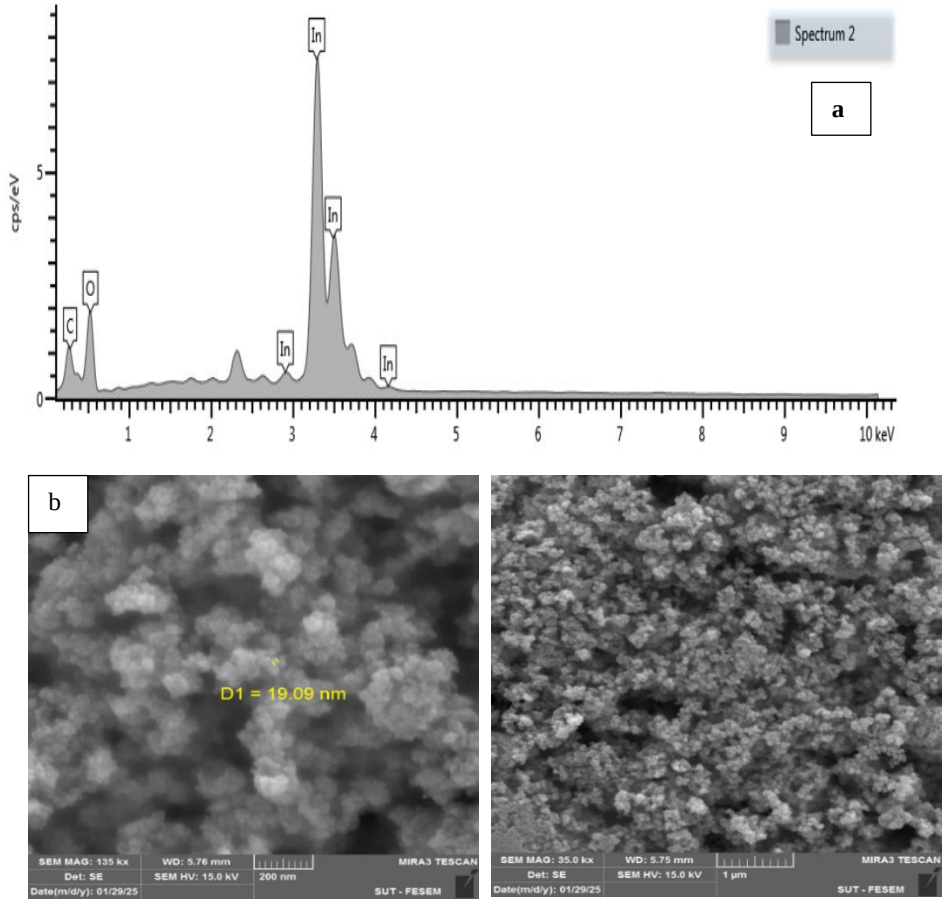


Figure 2. UV-Vis of $In@In_2O_3$ NPs.

EDX elemental analysis and morphological characterization of In@In_2O_3 nanoparticles by FESEM, TEM, and AFM

EDX (energy-dispersive X-ray spectroscopy), TEM (transmission electron microscopy), FESEM (field-emission scanning electron microscopy), and AFM (atomic force microscopy) were used to determine the size, shape, and composition of the resulting NPs. Figure 3(a) shows the EDX spectroscopy results, which confirmed the presence of indium and oxygen elements in the synthesized NPs with surface residues of carbon and oxygen. The oxygen is attributed to the thin indium oxide layer covering the indium NPs. In contrast, the carbon is attributed to the extract residues. The EDX results, together with FTIR, XRD, and TEM analyses, support the formation of the In@In_2O_3 core-shell structure. Figure 3(b) shows the FESEM results, which indicate that the prepared particles are irregularly spherical due to the residual extract on their surfaces and the thin oxide layer. Furthermore, TEM (Figure (c)) was used to measure the particles' dimensions and shape. Most particles were found to be irregularly spherical. The figure also illustrates the structure of the nucleus and shell; the contrast variation observed in the TEM image may be attributed to the difference in electron density between the metallic indium core and the surrounding In_2O_3 shell. Finally, the nanoscale size of the prepared particles was verified by AFM examination (Figure 3(d)). The average size, as determined by FESEM, TEM, and AFM, was approximately 10-60 nm.



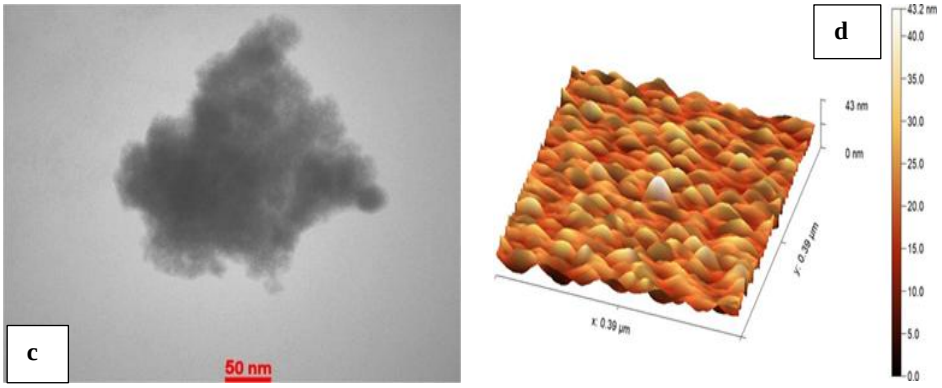


Figure. 3(a) EDX of In@In_2O_3 NPs, (b) FESEM of In@In_2O_3 NPs, (c) TEM of In@In_2O_3 NPs, (d) AFM of In@In_2O_3 NPs

X-ray diffraction (XRD)

Figure 4 shows the X-ray diffraction (XRD) pattern of biologically synthesized In@In_2O_3 NPs. The signals are attributed to the indium NPs with a tetragonal central phase, exhibiting a broad, dominant peak at 31.9°, representing level 101, and a set of peaks at 36.54°, 39.49°, 53.94°, 56.34°, 64.34°, 67.14° and 68.14°, representing levels 002, 110, 112, 200, 103, 211, and 202, which corresponds to card JCPDS card no. 05–0642. The weak signals (31.04, 35.04, 50.69, 59.74, and 60.89°), representing levels (222, 400, 440, 541, and 622), are attributed to cubic indium oxide reflections (JCPDS 06-0416). The broad background and noise are due to phytochemical residues from the plant extract used in the nanoparticle preparation. The presence of both metal and oxide phases in XRD analysis strongly supports the formation of a core-shell structure, consistent with previous studies demonstrating spontaneous surface oxidation of indium NPs [30].

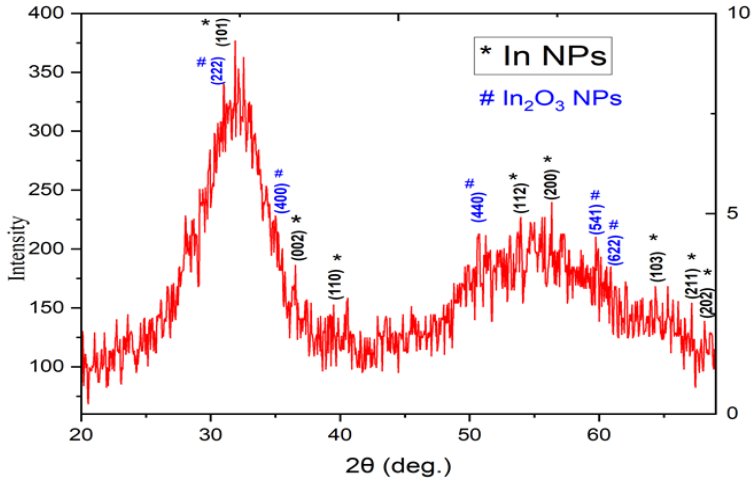


Figure.4 XRD of In@In_2O_3 NPs.

Brunauer-Emmett-Teller (BET)

A BET study was conducted to measure the surface area porosity. The surface area of the produced NPs was approximately 128.53 m^2/g. The H3 hysteresis loop observed in the adsorption-desorption equation is quite similar to that of the IUPAC type IV isotherm. The pore diameter is 6.46 nm on average, which is within the IUPAC-recommended range of 2-50 nm. The pore radius is 1.87 nm, and the pore volume is 0.2075 cm^3/g.

Zeta potential

Previous studies have reported that zeta potential values greater than +30 mV or lower than -30 mV generally indicate good colloidal stability due to strong electrostatic repulsion between NPs [31]. The zeta potential of the synthesized In@In_2O_3 NPs was -39.9 mV, indicating excellent colloidal stability and a low tendency for particle agglomeration. This high negative surface charge can be attributed to the phytochemical-mediated synthesis process, in which bioactive phytochemicals from the rosemary extract act as reducing, capping, and stabilizing agents. In addition, the oxide shell formed on the nanoparticle surface further contributes to the observed surface charge and stability.

Bioactivity of In@In_2O_3 NPs

Minimum inhibitory concentration (MIC)

To determine the minimum inhibitory concentration (MIC) and sub-minimum inhibitory concentration (Sub-MIC) of In@In_2O_3 NPs, four Gram-negative and Gram-positive bacterial strains were analyzed using a 96-well plate test with Mueller-Hinton broth and resazurin dye. The results demonstrated that the minimum inhibitory concentrations (MICs) for *S. aureus, E. faecalis, S. mutans, and E. coli* were 234.38 µg/mL, 234.38 µg/mL, 117.19 µg/mL, and 234.38 µg/mL, respectively. The sub-MICs were 117.19, 117.19, 58.60, and 117.19 µg/mL.

Toxicity

A straightforward and efficient method for quantifying hemolysis. Figure 5 illustrates the negative control group (N.C.), comprising RBCs in saline solution, which demonstrates a hemolysis rate of 0%. The positive control group (P.C.), consisting of 0.1% Triton X-100 and RBCs that underwent 100% hemolysis, indicated that the In@In_2O_3 NPs were non-toxic, resulting in 5.6% haemolysis.

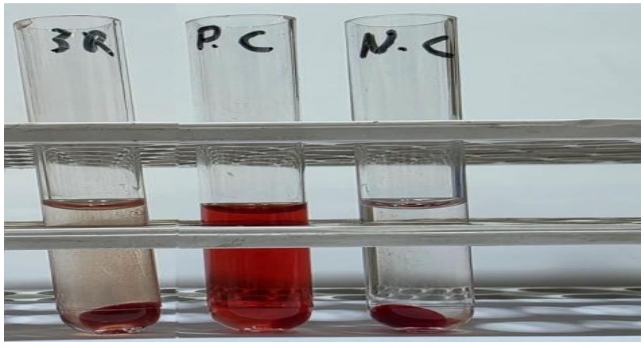


Figure.5 Toxicity of (3R), (P.C), and (N.C).

Biofilm and anti-biofilm activity

Biofilms were produced using 96-well microtiter plates. Their absorbance was subsequently quantified with a plate reader. The data indicate the robustness of the biofilm developed on the well surface. To evaluate anti-biofilm efficiency, a similar film approach was employed, utilizing diminished concentrations of the nanocomposites below the minimum inhibitory concentration (sub-MIC) during incubation. A reduction in absorbance relative to the untreated control was observed for all examined bacterial strains, thereby affirming anti-biofilm activity, as demonstrated in Figure 6 and Table 2.

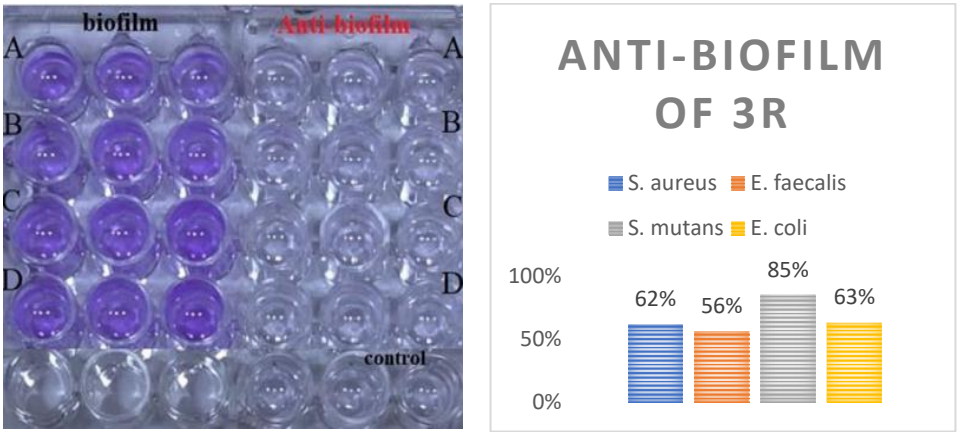


Figure 6. Control and biofilm, no treatment, and anti-biofilm treatment with In@In_2O_3 (3R) NPs for (A)*S. aureus*, (B) *E. faecalis*, (C) *S. mutans*, and (D) *E. coli.*

Table 2: Biofilm formation and anti-biofilm activity (Control Avg. reading (0.089)).

Isolates	Biofilm no treatment		Anti-biofilm of In@In_2O_3 NPs	
	Abs.	Result	Abs.	I
S. aureus	0.154	Weak	0.114	62%
E. faecalis	0.184	Moderate	0.131	56%
S. mutans	0.144	Weak	0.097	85%
E. coli	0.199	Moderate	0.130	63%

Antioxidant properties

For the purpose of determining the antioxidant properties of In@In_2O_3 NPs, the free radical 2,2-diphenyl-1-picrylhydrazyl (DPPH) was applied. Different amounts of In@In_2O_3 NPs were added to a combination of DPPH in equal proportions. The mixture was then blended with the In@In_2O_3 NPs solution. The findings indicated that, with increasing concentration levels, the inhibition percentage increases and the absorbance decreases, as shown in Figure 7 (a-e) and Table 3 below.

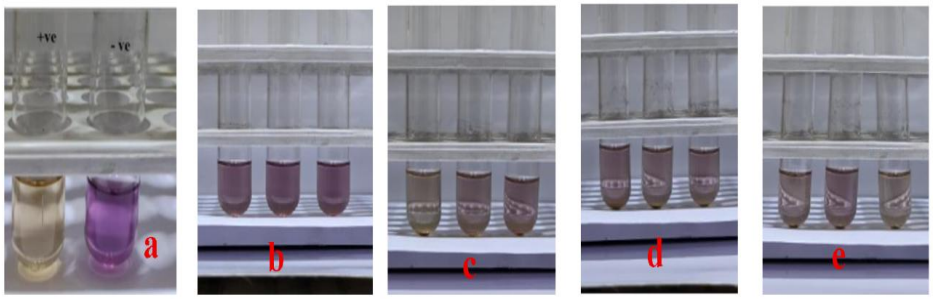


Figure. 7 (a) Positive control (DPPH and Vitamin C) and the negative control DPPH, antioxidant of (b) 25 µg/mL In@In_2O_3 NPs, (c) 50 µg/mL In@In_2O_3 NPs, (d) 75 µg/mL In@In_2O_3 NPs, (e) 100 µg/mL In@In_2O_3 NPs.

Table 3. Antioxidant properties of In@In_2O_3 NPs.

Conc. of In@In_2O_3 NPs	Abs.	I
25 µg/mL	0.576	51%
50 µg/mL	0.375	68%
75 µg/mL	0.351	70%
100 µg/mL	0.346	71%
DPPH	1.174	-

CONCLUSION

The objectives of this study included fabricating In@In_2O_3 NPs using environmentally friendly methods. The particles were evaluated using FTIR, UV-vis, XRD, EDX, FESEM, TEM, AFM, BET, and Zeta potential. The particles had an irregular spherical shape, with an average size of 10-60 nm and an approximate surface area of 128.53 m^2/g. IUPAC classification revealed an H3 hysteresis loop in the adsorption-absorption equation, similar to a type IV heat equation. The research showed that the particles were stable and evenly distributed in the dispersed liquid. According to the antibacterial activity study, the In@In_2O_3 NPs exhibited antimicrobial activity against the tested bacteria. The minimum inhibitory concentration (MIC) of 234.38 µg/mL was used in the erythrocytosis test for these particles, the highest value tested. In@In_2O_3 NPs disintegrated only a small percentage of red blood cells, demonstrating their non-toxicity, consistent with previous research. Furthermore, biofilms were generated in the research bacteria, and their antibacterial activity was tested using In@In_2O_3 NPs. The prepared particles prevented the formation of biofilms that contribute to antibiotic resistance. Finally, results from a DPPH (2,2-diphenyl-1-picrylhydrazyl) assay assessing the antioxidant activity of In@In_2O_3 NPs indicated that increasing their concentration enhances this activity.

ACKNOWLEDGEMENTS

The authors thank the Department of Chemistry, College of Education for Pure Science (Ibn Al-Haitham), University in Baghdad, Iraq, for providing the necessary resources to complete this research project.

Conflict of interest

The authors declare no conflicts of interest.

Ethical approval

Because the study raised no ethical issues or concerns, ethics approval was not required.

Data availability

Peer reviewers can access the data upon request.

Funding declaration

There was no funding for this study.

REFERENCES

1. Osman, M.E.; Dowidar, S.; Elsheikha, A.; Ragab, G.A. Green-synthesized Fe_2O_3 and $Ca(OH)_2$ nanoparticles alongside rosemary extract enhance growth, antioxidant defense, and secondary metabolite accumulation in Lupinus termis (Forssk.). *J. Soil Sci. Plant Nutr.* **2026**, 26, 4482-4503.
2. Xue, Y.; Ismail, A.J.B.; Lansing, M.G.; Mohd Hayati, M.F.B. Novel green synthesis of zinc oxide nanoparticles using *Salvia rosmarinus* extract for treatment of human lung cancer. *Open Chem.* **2023**, 21, 20230113.
3. Habeeb, T.H. Eco-friendly preparation of Co–Zn nanoparticles using rosemary extract and assessment of their antibacterial and antifungal activities. *Egypt. J. Bot*. **2026**, 66, 403-410.
4. Saeed, R.S.; Obead, K.A. Modified polyvinyl alcohol containing new imides/iron oxide nanoparticles: Synthesis, characterization and biological evaluation. *Iraqi J. Pharm. Sci.* **2025**, 34, 60-75.
5. Khalaf, S.F.; Al-Rashid, S.N.T. Size-dependent melting entropy and specific heat of metallic nanoparticles: A cohesive energy-based theoretical approach. *J. Nano part. Res.* **2025**, 27, 78.
6. Al-Hazmi, G.H.; Adam, A.M.; El-Desouky, M.G.; El-Bindary, A.A.; Alsuhaibani, A.M.; Refat, M.S. Efficient adsorption of Rhodamine B using a composite of Fe_3O_4@ZIF-8: Synthesis, characterization, modeling analysis, statistical physics and mechanism of interaction. *Bull. Chem. Soc. Ethiop.* **2023**, 37, 211-229.
7. Abood, N.H.; Merza, S.H. Preparation, kinetics and thermodynamic investigation of Janus green dye removal from aqueous solutions using MnO_2 nanoparticles as an adsorbent. *Bull. Chem. Soc. Ethiop.* **2025**, 39, 1509-1523.
8. Huseien, G.F. Potential applications of core-shell nanoparticles in construction industry revisited. *Appl. Nano.* **2023**, 4, 75-114.
9. Adam, A.; Mertz, D. Iron oxide@mesoporous silica core-shell nanoparticles as multimodal platforms for magnetic resonance imaging, magnetic hyperthermia, near-infrared light photothermia, and drug delivery. *Nanomaterials* **2023**, 13, 1342.
10. Zhao, B.; Yan, Z.; Liu, L.; Zhang, Y.; Guan, L.; Guo, X.; Li, R.; Che, R.; Zhang, R. A liquid-metal-assisted competitive galvanic reaction strategy toward indium/oxide core-shell nanoparticles with enhanced microwave absorption. *Adv. Funct. Mater*. **2024**, 34, 2314008.
11. Algawi, S.D.; Khalef, W.K.; Mohammed, S.R. Structure and morphological properties of In_2O_3 nanostructure prepared by pulse laser ablation method. *Iraqi J. Sci.* **2018**, 59, 1858-1865.
12. Zhong, F.G.; Yeh, C.L.; Chen, S.H. Enhanced photocatalytic activity of In/In_2O_3 core-shell nanowires synthesized via nanopatterned anodic aluminum oxide (AAO)-assisted casting and controlled-oxidation process. *Surf. Coat. Technol.* **2025**, 518, 132880.
13. van Spijk, J.N.; Schmitt, S.; Schoster, A. Infections caused by multidrug-resistant bacteria in an equine hospital (2012–2015). *Equine Vet. Educ.* **2019**, 31, 653-658.

14. Singh, D.; Rathod, V.; Ninganagouda, S.; Herimath, J.; Kulkarni, P. Biosynthesis of silver nanoparticles by endophytic fungi *Penicillium sp.* isolated from *Curcuma longa* and antibacterial activity. *J. Pharm. Res.* **2013**, 7, 448-453.
15. Bindu, S.; Oh, M.H.; Choi, C.H. Quorum sensing in Acinetobacter: Emphasis on antibiotic resistance, biofilm formation and quorum quenching. *AIMS Microbiol.* **2016**, 2, 27-41.
16. Gudikandula, K.; Vadapally, P.; Singara Charya, M.A. Biogenic synthesis of silver nanoparticles from white rot fungi: Characterization and antibacterial studies. *Open Nano.* **2017**, 2, 64-78.
17. Hamza, E.H.; El-Shawadfy, A.M.; Allam, A.A.; Hassanein, W.A. Study on pyoverdine and biofilm production with detection of LasR gene in MDR *Pseudomonas aeruginosa*. *Saudi J. Biol. Sci.* **2023**, 30, 103492.
18. Hu, C.; He, G.; Yang, Y.; Wang, N.; Zhang, Y.; Su, Y.; Zhao, F.; Wu, J.; Wang, L.; Lin, Y.; Shao, L. Nanomaterials regulate bacterial quorum sensing: Applications, mechanisms, and optimization strategies. *Adv. Sci.* **2024**, 11, 2306070.
19. Garong, C.J.; Burigsay, N.P.; Gapultos, R.S.; Mandawe, J.L.; Pedrosa, R.M.; Dayrit, G.B. Optimization of resazurin microplate assay (REMA) in evaluating anti-MRSA and anti-MSSA activities. *Acta Med Philipp.* **2025**, 59, 55.
20. Khan, M.; Naqvi, H.N.; Ahmad, M. Comparative study of cytotoxic and genotoxic potentials of zinc oxide and titanium dioxide nanoparticles. *Toxicol. Rep.* **2015**, 2, 765-774.
21. Jiang, L.; Yu,Y.; Li, Y.; Yu, Y.; Duan, J.; Zou, Y.; Li, Q.; Sun, Z. Oxidative damage and energy metabolism disorder contribute to the hemolytic effect of amorphous silica nanoparticles. *Nanoscale Res Lett.* **2016**,11, 57.
22. Jaffar, N.; Miyazaki, T.; Maeda, T. Biofilm formation of periodontal pathogens on hydroxyapatite surfaces: Implications for periodontium damage. *J. Biomed. Mater. Res. A* **2016**, 104, 2873-2880.
23. Kumar, A.; Bumunang, E.W.; Montso, P.K.; Singh, S.; Ateba, C.N. Multidrug-resistant virulent *Escherichia coli* strains in Cattle: Implications on food safety and public health. *Int. J. Microbiol.* **2025**, 2025, 9956724.
24. Sharifimehr, S.; Maley, J.; Ghosh, S. Development of faba protein-tannic acid conjugate via free radical grafting: Evaluation of interaction mechanisms and antioxidative properties. *Food Chem.* **2025**, 470,142508.
25. Rezanejad, R.; Omagh, S.M.; Heidarieh, M.; Raeisi, M.; Rafiee, G.; Alishahi, A.; Characterization of gamma-irradiated *Rosmarinus officinalis* L. (Rosemary). *Turk. J. Pharm. Sci.* **2018**,16, 43.
26. Nikolova, R.; Petrova, N.; Kostov-Kytin, V.; Titorenkova, R.; Petrov, P. Crystal chemistry of epsomite from three Bulgarian localities. *Geol. Balc.* **2025**, 54, 3-13.
27. Kulkarni, S.C.; Salunke, V.T.; Naeem, S.; Patil, A.V. Enhanced structural, optical and gas sensing properties of Zn-doped In_2O_3 nanomaterial synthesized via sol–gel technique. *Ceram. Int.* **2025**, 51, 12253-12261.
28. Ho, W.J.; Yang, H.Y.; Liu, J.J.; Lin, P.J.; Ho, C.H. Plasmonic effects of two-dimensional indium-nanoparticles embedded within SiO_2 anti-reflective coating on the performance of silicon solar cells. *Appl. Surf. Sci*. **2020**, 508, 145275.
29. Subramanian, S.; Neyvasagam, K.; Jenish, S.L.; Ganesh, V.; Yahia, I.S. Room-temperature ammonia gas sensor based on Ti-doped In_2O_3 thin film prepared by nebulizer spray pyrolysis. *J. Sol-Gel Sci. Technol.* **2025**,116,1008-1023.
30. Kelgenbaeva, Z.; Khandaker, J.I.; Ihara, H.; Omurzak, E.; Sulaimankulova, S.; Mashimo, T. Thermal and optical properties of In and In_2O_3 nanoparticles synthesized using pulsed plasma in water. *Phys. Status Solidi A* **2018**, 215, 1700910.
31. Nxumalo, K.A.; Adeyemi, J.O.; Leta, T.B.; Pfukwa, T.M.; Okafor, S.N.; Fawole, O.A. Antifungal properties and molecular docking of ZnO NPs mediated using medicinal plant extracts. *Sci. Rep*. **2024**,14, 18071.